Fuel-rich hetero-/homogeneous combustion of C$_3$H$_8$/O$_2$/N$_2$ mixtures over rhodium

John Mantzaras [a,*], Ran Sui [b], Rolf Bombach [c]

[a] *Laboratory for Scientific Computing and Modeling, Paul Scherrer Institute, CH-5232, Villigen, PSI, Switzerland*
[b] *Department of Mechanical and Aerospace Engineering, Missouri University of Science and Technology, Rolla, MO, 65409, United States*
[c] *Energy Systems Integration Platform, Paul Scherrer Institute, CH-5232, Villigen, PSI, Switzerland*

Abstract

The catalytic (heterogeneous) and gas-phase (homogeneous) combustion of C$_3$H$_8$/O$_2$/N$_2$ mixtures over rhodium was investigated experimentally and numerically at 5 bar and at fuel-rich equivalence ratios $\varphi = 2.0$-3.5 relevant to propane Catalytic Partial Oxidation (CPO). In situ spatially-resolved Raman measurements of major gas-phase species concentrations and Planar Laser Induced Fluorescence (PLIF) of formaldehyde were applied in an optically accessible channel-flow reactor to monitor the catalytic and gas-phase processes, respectively, while accompanying 2D simulations were carried out with detailed hetero-/homogeneous chemical reaction mechanisms. Due to the high gas-phase reactivity of propane, homogeneous chemistry could not be ignored over most of the reactor's oxidation zone length (upstream zone where the deficient reactant oxygen is not fully consumed). The presence of gas-phase chemistry deteriorated the otherwise high catalytic syngas (H$_2$ and CO) selectivities over the oxidation zone. Raman measurements of major gas-phase species concentrations over the restricted oxidation zone length without appreciable gas-phase chemistry showed that the catalytic reaction mechanism slightly underpredicted (overpredicted) the H$_2$ (CO) formation. The same behavior was also attested over the remaining length of the oxidation zone where combined catalytic and gas-phase chemistry was present. The production of considerable amounts of H$_2$ at the highest investigated equivalence ratio of 3.5 accelerated the onset of homogeneous ignition and the formation of strong flames. The discrepancies between measured and predicted homogeneous ignition distances were less than 6.8% in all cases, illustrating the validity of the employed hetero-/homogeneous kinetic schemes. Contrary to past methane CPO studies, the contribution of gas-phase chemistry and the formation of strong flames in propane CPO was detrimental to syngas production.

---

* Corresponding author.
E-mail address: ioannis.mantzaras@psi.ch (J. Mantzaras).

1. Introduction

Propane is an appreciable component (up to 4% vol.) in the abundant natural gas fuel and liquefies at modest pressures of ∼8 bar at room temperature, allowing for convenient storage and easy transport. Furthermore, Liquefied Petroleum Gas (LPG, a mixture of propane and butane) is widely available in compact containers and is hence a prime candidate for decentralized power generation [1]. Some important physicochemical properties of propane are shared by other high hydrocarbons, such as the negative temperature coefficient in the gas-phase oxidation rate [2] and the larger than unity Lewis number. The catalytic partial oxidation (CPO) of propane has attracted increased attention for Solid Oxide Fuel Cell (SOFC) portable power systems [3]. To circumvent direct use of propane or LPG that can cause strong carbon deposition (coking) and hence potential catalyst deactivation of the Ni-based SOFC anodes, the hydrocarbon fuels can be reformed via CPO to syngas (H_2 and CO). Compact propane CPO reformers for SOFCs were developed in [4].

Comparative studies of propane CPO on noble metals have shown that Rh gives the highest syngas selectivity, Pt forms more H_2O, Pd produces more solid carbon, while Ir strongly sinters [5]. Experiments of propane CPO over Rh confirmed the low coking propensity [6] and assessed the effects of support [7] and residence time [8] on syngas selectivities. Tests in an atmospheric-pressure isothermal annular microreactor have led to the evaluation of main kinetic parameters [9], while 1D axial profiles of species concentrations and temperature (acquired with a traversable microprobe) identified the different reaction zones during propane CPO at pressures up to 4 bar [10] and studied the impact of homogeneous chemistry at 1 bar [11]. Such 1D measurements have greatly facilitated kinetic analyses, although detailed simulations of the probe's intrusive effects suggested that they could cause appreciable errors -particularly at non-isothermal conditions [12]. Finally, in atmospheric-pressure propane CPO over Rh, extinction limits were deduced in a heat recirculating reactor [13] and 1D microprobe measurements above a stagnation point-flow reactor led to the development of a detailed catalytic reaction mechanism [14].

Notwithstanding the significant progress achieved with 1D axial-profile measurements, only 2D measurements can unequivocally assess the true state of catalytic reactions (i.e., kinetically-controlled, transport-controlled, or mixed kinetically/transport controlled regimes) by evaluating profiles of the deficient reactant normal to the catalyst surface. 2D non-intrusive species concentration measurements over Rh were reported in earlier methane CPO [15,16] and

propane catalytic total oxidation (CTO) [17] studies. Furthermore, 2D measurements are crucial in determining the gas-phase chemical processes, given the strong dependence of homogeneous ignition on the boundary layer species and temperature profiles [18], and the increase of the gaseous propane reaction rates with pressure due to their ∼p^2 dependence.

The present work investigates experimentally and numerically the CPO of propane over Rh at 5 bar. Experiments are performed in an optically accessible reactor, whereby the heterogeneous processes are evaluated with in situ 2D Raman measurements and the gas-phase processes are monitored with Planar Laser Induced Fluorescence (PLIF) of formaldehyde. Main objectives are to study the coupling of catalytic and gas-phase chemistry during propane CPO, and assess the conditions leading to the onset of homogeneous ignition and flame formation.

2. Experimental

2.1. High-pressure test rig

The channel-flow reactor was made of two 9-mm-thick horizontal ceramic (Si[SiC]) plates (with length (-x), width (-z) and transverse separation (-y) of 300 mm, 104 mm and 7 mm, respectively) and two 5-mm-thick vertical quartz glass windows (see Fig. 1 and for details [19,20]). Plasma vapor deposition (PVD) was employed to coat the two 300×104 mm^2 inner Si[SiC] surfaces; a 1.5-μm-thick non-porous Al_2O_3 layer was applied first, followed by a 2.2-μm-thick Rh layer. The Al_2O_3 coating mitigated chemical interactions between Si and Rh. Moreover, the appreciably thick noble metal layer closely resembled a polycrystalline Rh surface, while the absence of bulk Si or Al from the catalyst surface was confirmed with post-combustion X-ray Photoelectron Spectroscopy (XPS).

The reactor was placed inside a high-pressure cylindrical steel vessel. Two 35-mm-thick and 350-mm-long quartz glass windows on the vessel provided optical access to both 300×7 mm^2 reactor sides (Fig. 1a). Moreover, two circular quartz windows at the reactor exhaust and the back vessel flange yielded streamwise optical access for the H_2CO-PLIF beam. The catalyst surface temperatures were monitored by 12 (for each plate) S-type thermocouples, placed along the x-y symmetry plane (Fig. 1) and affixed 0.9 mm beneath the catalyst through 8.1-mm-deep and 1.2-mm-diameter holes eroded from the outer Si[SiC] surfaces. Two adjustable-power resistive coils were positioned above/beneath the two Si[SiC] plates over the length $100 < x < 300$ mm (Fig. 1b) to counter external heat losses at the reactor rear. Given the high gaseous reactivity of propane, and in order to
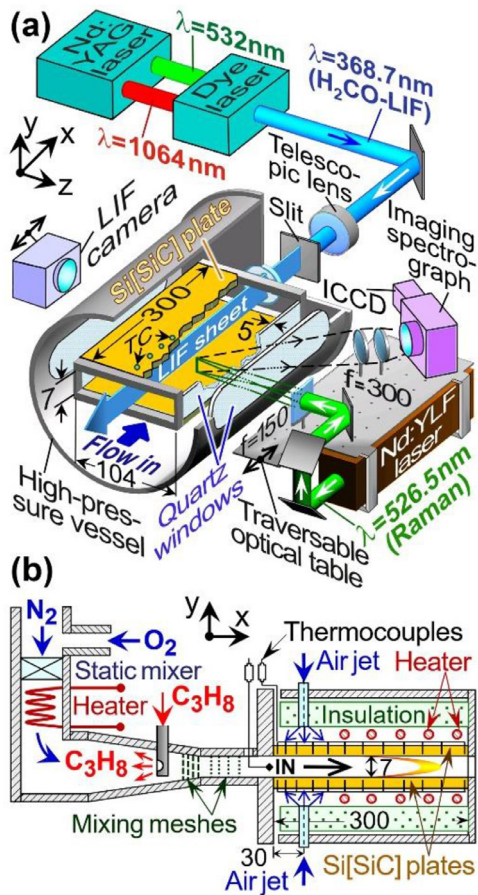
Fig. 1. (a) Test-rig and Raman/PLIF setup, (b) reactor details (all distances are in mm).

delay the onset of homogeneous ignition, two adjustable air-jet flows (located at $x = 30$ mm, Fig. 1b) impinged vertically on the outer Si[SiC] surfaces to cool the reactor front.

Batteries delivered C_3H_8 (99.95% purity), O_2 and N_2, and three Brooks mass flowmeters controlled the gas flows. N_2 was mixed with O_2 and the mixture was electrically preheated. Propane was injected counterflow to the preheated O_2/N_2 stream (Fig. 1b) in a 200-mm-long conical section. Therein, 8 wire meshes (0.5 mm² open area) yielded a uniform flow and a good mixing of C_3H_8 with O_2/N_2. Optimization of the mesh positions was achieved with suitable measurements at the exit of the conical section: hot wire velocimetry assessed the flow uniformity, while NO-PLIF (100 ppm NO added into the C_3H_8 stream, excitation at 226.25 nm and detection at 240-265 nm) confirmed the good mixing quality. The gas inlet temperature ($x = 0$, marked "IN" in Fig. 1b) was measured with a radiation-shielded K thermocouple.

2.2. Laser based measurements

The Raman/PLIF setups are illustrated in Fig. 1a. For Raman, excitation was provided by a frequency-doubled Nd:YLF laser (Quantronix Darwin-Duo, 2.4 kHz repetition frequency, radiation at 526.5 nm), producing a beam with pulse energy and duration of 30 mJ and 130 ns, respectively. The beam was focused by an $f = 150$ mm cylindrical lens to a 0.3-mm-thick vertical line (Fig. 1a), which encompassed the 7 mm channel height and was offset laterally (-z) 15 mm from x-y symmetry plane in order to improve the light collection angle and diminish thermal beam steering (as in past studies [17,18]). Two spherical lenses ($f = 300$ mm) collected the scattered light and focused it into a 25 cm imaging spectrograph (Chromex-250i, with a Princeton Instruments PI-MAX1024GIII ICCD camera). The camera recorded images of 640×255 pixels, corresponding to Raman spectral shift and y-direction, respectively. The 7-mm height was resolved with 220 pixels that were finally binned to 64 pixels.

To suppress light collection from the excitation radiation, a tilted holographic notch filter (Kaiser-Optical-Systems 532 nm) and a glass filter (OG550 Schott) were placed at the ICCD lens. A traversable optical table housed the Nd:YLF laser, the spectrograph and all optics (Fig. 1a), permitting Raman measurements over the extent $8 \leq x \leq 124$ mm. Light from 350,000 laser pulses was integrated on the ICCD chip to enhance the signal-to-noise ratio. Effective Raman cross-sections (accounting for transmission efficiencies from the camera, lenses, spectrometer, windows and filters) were determined by recording signals from pressurized C_3H_8, N_2 and O_2. For species concentrations $\geq 3\%$ volume the measurement accuracy was $\pm 4\%$, while for concentrations down to 0.5% volume the accuracy dropped to $\pm 10\%$; lower concentrations could not be effectively resolved. Due to low signal-to-noise ratios, measurements closer than 0.5-0.7 mm from the catalyst were disregarded.

Homogeneous combustion was monitored with PLIF. Given that OH-PLIF was not amenable at the CPO-relevant fuel-rich stoichiometries, H_2CO-LIF was employed –as in past methane CPO studies [15,16]. The 532 nm radiation of an Nd:YAG laser (Quantel YG781C20-CL-D-LNE3, 10 ns pulse duration, 20 Hz repetition rate) pumped an Rh6G dye laser (Quantel TDL90-NBP2EWT-UVT3), whose output was frequency-mixed with the residual fundamental Nd:YAG radiation (1064 nm) to produce an excitation beam at 368.7 nm (∼15 mJ/pulse). H_2CO transitions near the ${}^RR$ (A-X) 4_1^0 hot band were excited, warranting strong signals at elevated temperatures. The excitation beam was transformed into a vertical light sheet by a telescopic lens and a slit mask, which propagated counterflow along the reactor's x-y symmetry plane (Fig. 1a). The quite wide light

sheet (∼10 cm, before entering the vessel) together with the low oscillator strength and high intrinsic quenching of carbonyl compounds precluded saturation of the fluorescence signal.

A gated ICCD camera (LaVision Imager Compact HiRes-IRO, 1392 × 1024 pixels binned to 696 × 512) recorded the fluorescence emission at 90° through the high-pressure vessel and reactor side-windows (Fig. 1a). The spectral range 400-480 nm of the total H_2CO fluorescence emission (400-550 nm) was collected by positioning an OMEGA 440BP80 interference filter in front of an $f105mm/2.8$ lens of the ICCD. Areas of 100 × 7 mm^2 were recorded on 1360 × 70 pixels. To map the entire 300 × 7 mm^2 channel area, the ICCD camera was traversed axially in 60 mm steps. To increase the signal-to-noise ratio (and given the steady operating conditions), 280 PLIF images were averaged at each position.

3. Numerical

A 2-D steady Navier-Stokes CFD code [19,20] simulated the 300 × 7 mm^2 channel domain on the *x-y* symmetry plane. An orthogonal staggered mesh with 820 × 72 points (in -*x* and -*y*, respectively) provided grid-independent solutions (key requirement was the independence of homogeneous ignition and outlet species compositions on grid size). The lower-wall ($y = 0$) and upper-wall ($y = 7$ mm) temperatures were prescribed, by fitting curves through the 12 thermocouple measurements on each plate. All properties at the inlet ($x = 0$) were uniform.

For heterogeneous chemistry, the detailed mechanism from Karakaya and Deutschmann [14] was employed (7 gaseous and 17 surface species), which has been validated against atmospheric-pressure propane CPO measurements. For gaseous chemistry, the San Diego mechanism was used (58 species, 268 reactions) with its accompanying transport and thermodynamic databases [21]. The heterogeneous and homogeneous reaction rates were computed using Chemkin [22,23], while a mixture-averaged transport model was adopted with thermal diffusion for H and H_2 [24].

4. Results and discussion

Experiments were performed at C_3H_8-to-O_2 equivalence ratios $\varphi = 2.0$-3.5 (see Table 1), with $\varphi = 3.33$ being the theoretically optimal stoichiometry for syngas production (O_2-to-C_3H_8 volumetric ratio of 1.5). Similar to our past methane CPO study [15], the pressure was fixed to 5 bar (high enough for a strong Raman signal and still low enough to minimize beam steering). The preheat was modest (360-380 K), while the inflow velocities

Table 1
Experimental conditions[a].

Case	φ	U_{IN}	T_{IN}	C_3H_8	O_2
1	2.0	0.38	360	7.7	19.2
2	2.5	0.33	369	9.0	18.0
3	3.0	0.41	369	11.4	19.0
4	3.0	0.30	365	11.4	19.0
5	3.5	0.30	376	14.6	20.8
6	3.5	0.21	380	14.6	20.8

[a] Equivalence ratio, inlet velocity (m/s), inlet temperature (K), inlet vol. content (%) of C_3H_8 and O_2 (balance N_2).

were altered to better control the onset of homogeneous ignition. The 20 K preheat differences reflected the varying heat feedback towards the inlet, due to the different equivalence ratios. The flows were laminar, with inlet Reynolds numbers 340-680 based on the channel height.

4.1. Raman measurements and simulations

Comparisons between measured and simulated transverse (-*y*) profiles of $C_3H_8/O_2/H_2/CO/H_2O/CO_2$ mole fractions at six selected streamwise positions over $8 \leq x \leq 124$ mm are shown in Fig. 2 for Case 5 ($\varphi = 3.5$). Corresponding profiles of the reactants and CPO products H_2 and CO for Case 4 ($\varphi = 3.0$) are depicted in Fig. 3, while for Case 2 ($\varphi = 2.5$) the H_2 and CO are plotted in Fig. 4. The axial extent in Figs. 2-4 falls within the oxidation zone of the reactor, i.e., where the deficient reactant O_2 is not fully consumed. The measured wall temperatures for the above cases ranged from 932 to 1134 K (see Fig. 5); wall temperatures for the remaining cases are included in Fig. S1. In Figs. 5 and S1, the computed streamwise profiles of the catalytic (*C*) and gas-phase (*G*) propane conversion rates are also given (negative rates signify consumption). The *C* rates refer to the contribution of both catalytic walls, while the *G* rates were calculated by integrating the volumetric gaseous rates over the 7-mm channel height.

Despite the efficient air-jet cooling at the reactor front, the species profiles in Figs. 2-4 were strongly affected by gaseous chemistry. The coexistence of the *C* and *G* propane conversions in Fig. 5, over most of the Raman measurement extent ($8 < x < 124$ mm), attested the importance of both reaction pathways. This was further evident by comparing in Fig. S2 the C_3H_8 and H_2 mole fractions near the lower wall for positions $x \leq 66$ mm, using simulations with hetero-/homogeneous chemistry and with only heterogeneous chemistry. In the latter simulations, the C_3H_8 conversion was lower and the H_2 production higher. For $\varphi = 3.5$, only the $x = 8$ mm profiles coincided, while at $x = 66$ mm the differences in C_3H_8 and H_2 wall mole fractions were 40% and 50% re-
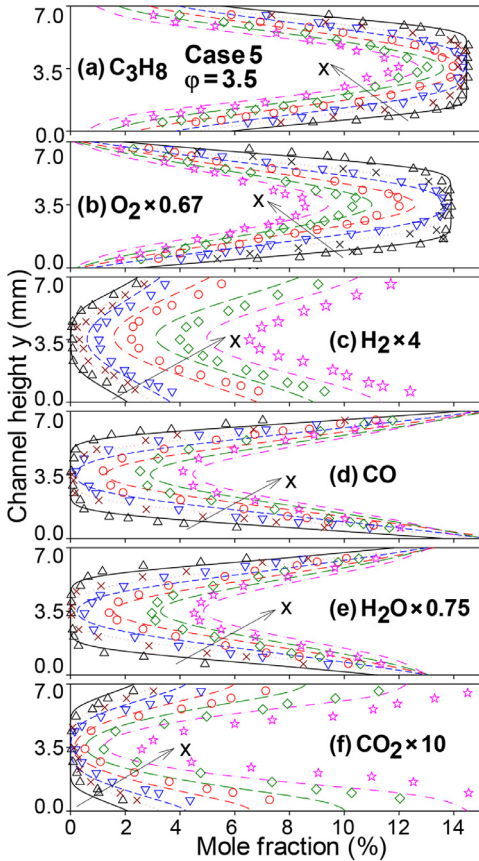
Fig. 2. Mole fraction transverse profiles (lines: simulations, symbols: Raman measurements) for Case 5: $x = 8$ (solid lines, upper-triangles), 21 (dotted lines, crosses), 36 (short dashed lines, lower-triangles), 66 (dashed-dotted lines, circles), 96 (long dashed lines, diamonds), and 124 mm (dashed-double-dotted lines, stars).

spectively (Fig. S2c); at the last Raman-measuring position $x = 124$ mm, the corresponding differences grew to 106% and 286%. For $\varphi = 2.5$, the differences were smaller (Fig. S2a) but still homogeneous chemistry was appreciable for $x > 21$ mm. It is hence apparent that propane CPO is a combined hetero-/homogeneous process, as also hinted in past 1D microprobe experiments [11,14]. This is in stark contrast to our earlier methane CPO studies [15], whereby a pure heterogeneous reaction zone up to $x = 66$ mm could be identified for near-optimal CPO stoichiometries and up to $x = 100$ mm for lower stoichiometries. Moreover, these differences occurred despite the fact that in methane-CPO [15] the (non-cooled) wall temperatures were up to 180 K higher over $x < 66$ mm and the gas inlet temperatures were ~80 K higher than the present propane values.
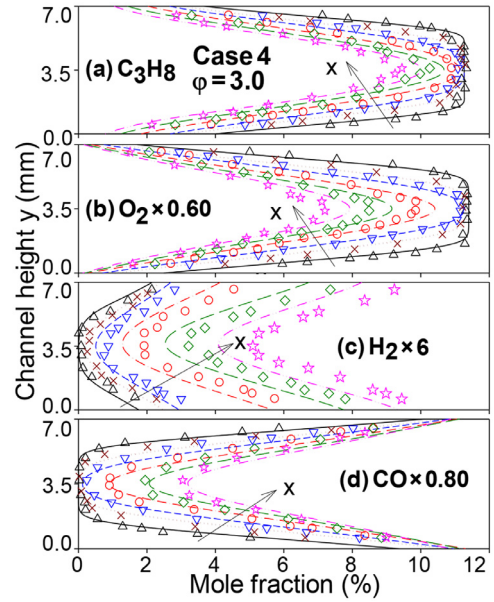

Fig. 3. Mole-fraction transverse profiles for Case 4. Notation of lines and symbols as in Fig. 2.
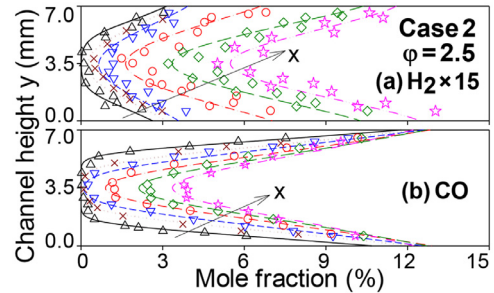

Fig. 4. Mole-fraction transverse profiles for Case 2. Notation of lines and symbols as in Fig. 2.
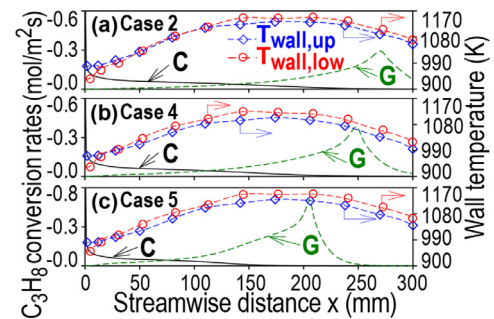

Fig. 5. Measured wall temperatures for Cases 2, 4, 5 and simulated axial profiles of catalytic (C) and gaseous (G) propane conversion rates.

The comparisons between measurements and simulations in Figs. 2 and 3 were quite favorable, although the H_2 (H_2O) production was somewhat underpredicted (overpredicted) and the CO (CO_2) production somewhat overpredicted (underpredicted). For $\varphi = 2.5$ in Fig. 4, there was a meager H_2 production and this resulted in a larger measurement scatter.

The deficient reactant O_2 approached transport-limited conversion as demonstrated by the low wall-to-center O_2 mole-fraction ratios in Figs. 2 and 3, which ranged from 1% to 20%; the same was also attested in all other cases. This behavior was further supported by the measurements, despite the absence of Raman data 0.5-0.7 mm from both walls. Nonetheless, the first 2–3 axial positions in Figs. 2-3 with corresponding ratios 10%-20% fell into the mixed transport/kinetics regime, and this could only be asserted with the present transverse measurements (past propane-CPO axial species measurements only suggested a transport-limited O_2 conversion [10]).

Surface characterization was accomplished by Scanning Electron Microscopy (SEM), Energy Dispersive X-Ray (EDX) and X-ray Photoelectron Spectroscopy (XPS), performed ex-situ on samples at room-temperature and heated to 1000 K. The 1000 K was representative of the wall temperatures over the extent of Raman measurements in Figs. 2-4. The XPS spectra in Fig. S3a showed that, in the presence of O_2, the Rh_2O_3 (Rh^{+3}) phase was dominant at 1000 K as opposed to metallic Rh^0 phase at 293 K. The increased oxidation state at 1000 K was further corroborated by the EDX measurements in Fig. S3b.

4.2. Hetero-/homogeneous chemistry coupling

The hetero-/homogeneous chemistry coupling is elaborated using Case 5 as reference case. Transversely-averaged streamwise profiles of species mole fractions are illustrated in Fig. 6 for two simulations: with hetero-/homogeneous chemistry ($C + G$) and with only heterogeneous chemistry (C). For the $C + G$ simulation of Case 5, streamwise profiles of the catalytic (C) and gaseous (G) conversion rates (the G rates are integrated over the 7-mm-height) are provided in Fig. 7.

Gaseous chemistry has a strong contribution, as manifested by the large G conversions in Fig. 7. This is also evident by the appreciable differences between the two simulated mole fraction profiles in Fig. 6. The onset of vigorous homogeneous combustion (flame) was defined as the axial location (x_{ig}) of the computed peak H_2CO mole fraction in Fig. 6, which was in turn close to the peak G_{H2CO} production (peak positive rate in Fig. 7); both nearly coincided, yielding $x_{ig} \approx 205$ mm. The extent $x < x_{ig}$ encompassed the oxidation zone (with O_2 still present, see Fig. 6); therein C_3H_8 and O_2 were converted by both C and G pathways while
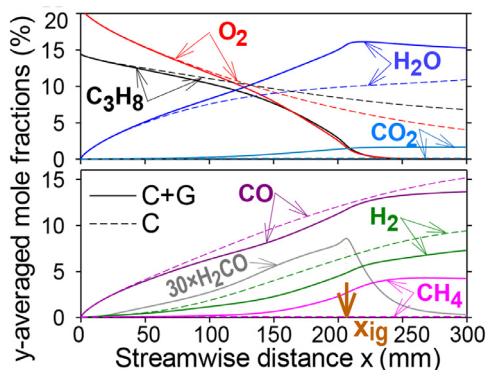

Fig. 6. Simulated streamwise profiles of transversely-averaged species mole fractions for Case 5. Solid lines: hetero-/homogeneous chemistry ($C + G$), dashed lines: heterogeneous chemistry (C).
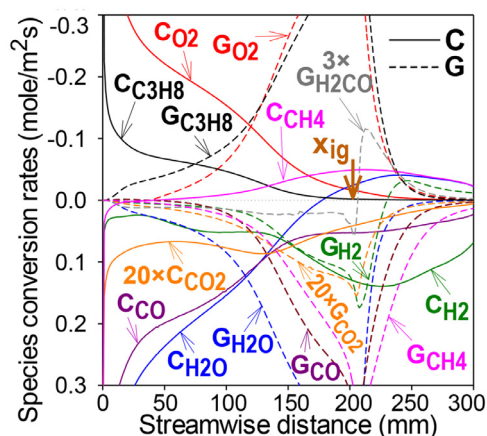

Fig. 7. Simulated catalytic (C, solid lines) and gaseous (G, dashed lines) species conversion rates for Case 5.

the main partial and total oxidation products (H_2, CO, H_2O, CO_2) were produced again by both pathways. Methane was the only intermediate gas-phase species in the catalytic reaction mechanism [14], but over most of the length $x < x_{ig}$ its production predominantly came via G while C acted as a sink by adsorbing the gaseous-produced methane (Fig. 7).

While H_2 and CO were produced by both catalytic and gaseous pathways over $x < x_{ig}$ (Fig. 7), the $C + G$ simulation in Fig. 6 indicated lower mole fractions for these products compared to the only-C simulation. This was because the gaseous pathway accelerated the consumption of C_3H_8 but in a way favoring formation of total oxidation products (see the greater H_2O and CO_2 mole fractions in the $C + G$ simulation of Fig. 6). This was further verified by monitoring the ratios of O_2-to-C_3H_8 catalytic molar conversions; for $0 < x < x_{ig}$, the C_{O2}/C_{C3H8} ratio in the $C + G$ simulation was on the
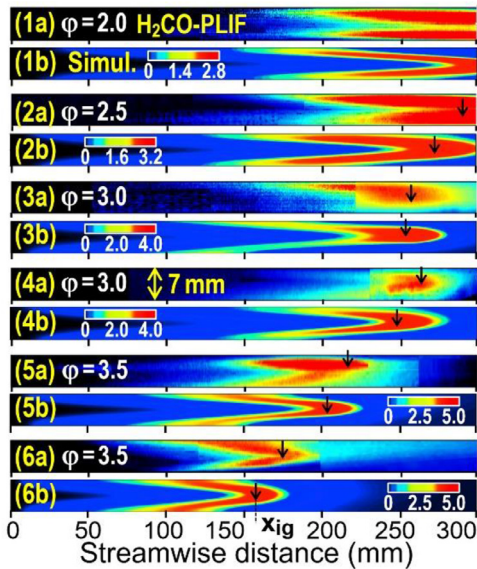
Fig. 8. Formaldehyde maps for Cases 1-6: (a) PLIF measurements, (b) simulations. Color bars provide the computed H_2CO ($1000 \times$ ppmv) and vertical arrows define the homogeneous ignition locations (x_{ig}).

Fig. 9. Simulated catalytic (C) and gaseous (G) conversion rates of O_2 for Case 6, at four different wall temperatures.

average 3.3, while in the only-C simulation it was 2.5, i.e. closer to the ideal CPO ratio of 1.5 rather than to the total oxidation (CTO) ratio of 5.

In the oxidation zone, the gaseous pathway converted C_3H_8 by radical attack reactions, which at the same time produced H_2, while CO was mainly produced via HCO hydrogen abstraction reactions (see Fig. S4a for the most significant C_3H_8, H_2 and CO reactions at $x = 100$ mm). The catalytic adsorption/desorption reactions of C_3H_8, H_2 and CO were partially equilibrated over the entire oxidation zone, with the net catalytic rates being much smaller than either the adsorption or desorption rates.

Finally, over the Raman measurement extent ($x \leq 124$ mm), potential spectral interferences were marginal (it is noted that the propane Raman signal window encompasses all C-H stretch vibrations in saturated and unsaturated hydrocarbons). All other hydrocarbon species had much lower mole fractions than C_3H_8: C_2H_4 by a factor of 1.5×10^4, C_3H_6 by 6.2×10^3 and CH_4 by 2.1×10^3 at $x = 8$ mm; these factors decreased to 10, 25 and 30, respectively, at the last Raman measuring location $x = 124$ mm. Only close to homogeneous ignition ($x_{ig} = 205$ mm) C_2H_4 and CH_4 overtook the C_3H_8 mole fraction.

4.3. Homogeneous ignition

Simulated and PLIF-measured H_2CO distributions are compared in Fig. 8. The homogeneous ig-
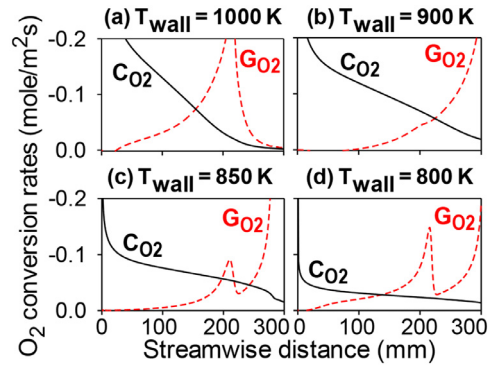
nition positions x_{ig} (marked with arrows in Fig. 8) were defined in the simulations as outlined in Section 4.2; a similar procedure was adopted for the PLIF images using the measured intensity counts. The color differentiation in the PLIF images reflected different settings in the ICCD camera; however, this did not affect the unambiguous determination of homogeneous ignition. For Case 1, homogeneous ignition could not be assessed since only the upstream part of the flame was inside the channel. A strong two-dimensionality of the flames is evident in Fig. 8, showing the advantages of the present 2D model approach. The agreement between simulated and measured x_{ig} and flame lengths was quite good for Cases 2-6. The simulations underpredicted mildly homogeneous ignition (by up to 6.8%). For example, in Cases 2 and 6 the predicted x_{ig} were 272 mm and 158 mm while the measured ones were 290 mm and 168 mm, respectively. There were nevertheless some small differences, as the simulated formaldehyde in the preflame regions was confined into thin reaction zones, while the PLIF resulted in broader distributions. This behavior was also reported in [15,16] and has been ascribed [25] to the strong signal originating from the colder, high-density regions ahead of the flame.

The homogeneous ignition distances in coupled hetero-/homogeneous combustion largely reflected gas-phase ignition characteristics and were inversely proportional to suitably-defined gaseous reaction times [18]. Interestingly, homogeneous ignition was particularly favored at the higher equivalence ratio Cases 5 and 6 (they had the shortest x_{ig}). This happened despite the following facts: a) over the gaseous induction zones $0 < x < x_{ig}$, Cases 5 and 6 had slightly lower wall temperatures than the other cases (see Figs. 5 and S1), and b) rich propane mixtures ignite harder (ignition delays become longer with increasing equivalence ratio [26]). This unexpected behavior was a result of the H_2

produced via the catalytic pathway over the gaseous induction zones. To illustrate this, additional simulations were made by replacing H_2 in the catalytic mechanism with an artificial H_2^* species that had the same transport and thermodynamic properties as H_2, but did not participate in any gaseous reaction. This change left practically unaffected the low-φ flames in Cases 1 and 2, for which little H_2 was produced catalytically (Fig. 4). However, it substantially affected ignition of the $\varphi = 3.5$ Cases 5 and 6 that had appreciable H_2 catalytic production (see Figs. 2 and 7). For example, simulations with H_2^* yielded $x_{ig} = 246$ mm and 182 mm for Cases 5 and 6, substantially longer than the simulations in Fig. 8 with corresponding $x_{ig} = 205$ mm and 158 mm. This indicated an important and CPO-specific hetero-/homogeneous chemistry coupling via H_2 that in turn affected the radical pool buildup in the gaseous induction zone. In contrast, during fuel-lean combustion of $C_3H_8/O_2/N_2$ mixtures over Rh, the hetero-/homogeneous chemistry coupling had a much weaker effect, with CO being the most important intermediate [27].

Following homogeneous ignition, catalytic reforming reactions consumed H_2O and CH_4 and produced H_2 and CO (Fig. 7). On the other hand, gas-phase reactions always produced CH_4 and CO, while H_2 was produced via G until shortly downstream x_{ig} and then consumed (Fig. 7). The key gas-phase reactions affecting CH_4, CO and H_2 at $x = 290$ mm are provided in Fig. S4b, showing that the main step producing CH_4 and consuming H_2 was $H_2+CH_3=CH_4+H$ (reverse of R41).

Contrary to past CH_4-CPO studies [15], where (under similar flow conditions) gas-phase chemistry increased the syngas (H_2 and CO) production, in C_3H_8-CPO gas-phase chemistry reduced the syngas yields (see Fig. 6). This was not a result of slower post-ignition ($x > x_{ig}$) gaseous reforming chemistry, because in both C_3H_8-CPO and CH_4-CPO these gaseous reactions were nearly equally fast (as assessed via constant-pressure batch reactor simulations using the Senkin package of Chemkin [28]). The reason for the lower syngas production was the appreciable contribution of C_3H_8 gaseous chemistry in the far upstream parts of the oxidation zone ($x << x_{ig}$), which spoiled the high catalytic selectivities towards H_2 and CO as exemplified in Fig. 6. The aforementioned increased gas-phase contribution in the C_3H_8-CPO oxidation zone was largely absent in CH_4-CPO. It is also noted that since both C_3H_8-CPO and CH_4-CPO are eventually equilibrium-limited and not kinetically-limited processes [10,14], the aforementioned interplay of catalytic and gaseous chemistry affects the syngas yields at reactor residence times (or reactor lengths) that are not too long for equilibrium. Such short contact time reactors for CPO of hydrocarbons are typically encountered in power generation [29].
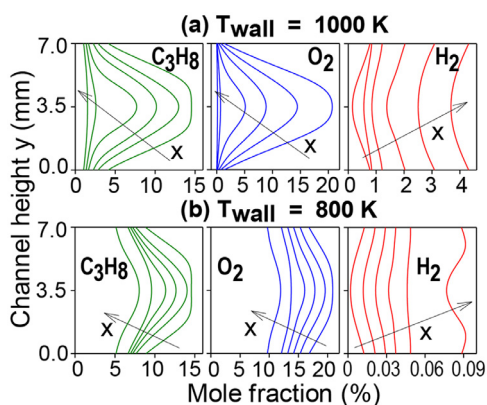

Fig. 10. Simulated transverse profiles of C_3H_8, O_2 and H_2 mole fractions for Case 6 at two different wall temperatures and six axial positions. The arrows indicate the direction of increasing axial distance ($x = 21, 85, 150, 200, 240$ and 300 mm).

Finally, the impact of wall temperature on homogeneous chemistry has been investigated numerically. Case 6 was simulated under a constant wall temperature (T_w) boundary condition, with T_w ranging from 800 K to 1000 K in increments of 50 K. The transversely-averaged catalytic and gas-phase conversions of the deficient reactant O_2 are provided in Fig. 9 for four wall temperatures. It is seen that even for the lowest $T_w = 800$ K, gas-phase chemistry cannot be neglected. Furthermore, for $T_w = 850$ K and 800 K a two-stage gas-phase propane ignition [2] is manifested by the G_{O_2} profiles. The reason for the resilience of gas-phase chemistry at T_w as low as 800 K is illustrated in Fig. 10. In Fig. 10b the transverse species profiles indicate increased amounts of the reactants C_3H_8 and O_2 near the wall at $T_w = 800$ K due to the slower catalytic chemistry; this near-wall reactant excess, in turn, promotes homogeneous combustion. On the other hand, for $T_w = 1000$ K the amount of reactants C_3H_8 and O_2 near the wall is much reduced (Fig. 10a), but this is compensated by the higher wall temperature that facilitates the onset of homogeneous ignition.

Even though gas-phase chemistry remains significant for T_w down to 800 K, the CPO functionality of the catalyst ceases below ∼900 K. Fig. 10 shows that while the average outlet ($x = 300$ mm) H_2 mole fraction is 4% at $T_w = 1000$ K, it drops to only 0.085% at $T_w = 800$ K. The detailed simulations showed that already at $T_w = 900$ K the outlet H_2 mole fraction drops below 0.5% (this result holds for either hetero-/homogeneous chemistry simulation or only heterogeneous chemistry simulation). There-

fore, for all CPO-relevant wall temperatures, gas-phase chemistry cannot be neglected at the present channel confinement of 7 mm and pressure of 5 bar.

5. Conclusions

The fuel-rich hetero-/homogeneous combustion and the CPO of propane to syngas over Rh was investigated in a catalytic channel-flow reactor at 5 bar using in situ Raman and formaldehyde-PLIF measurements, accompanied by 2D simulations with detailed catalytic and gas-phase chemistry. Gaseous chemistry could not be neglected in the oxidation zone of the reactor, resulting in reduced syngas production. Raman measurements of major gas-phase species concentrations over the reactor length without appreciable gas-phase chemistry indicated that the catalytic reaction mechanism slightly underpredicted (overpredicted) the H_2 (CO) formation. Production of appreciable amounts of H_2 at the highest equivalence ratio of 3.5 accelerated substantially homogeneous ignition and flame formation. The predicted and PLIF-measured homogeneous ignition distances had differences within 6.8%, attesting the aptness of the employed kinetic schemes. Contrary to CH_4-CPO, the presence of gas-phase chemistry in the oxidation zone and the subsequent formation of strong flames in C_3H_8-CPO were detrimental to syngas production. For all CPO-relevant wall temperatures ($T_w > 900$ K) that result in appreciable syngas production, the impact of gaseous chemistry could not be ignored.

Declaration of Competing Interest

The authors declare that they have no known competing financial interests or personal relationships that could have appeared to influence the work reported in this paper.

Acknowledgements

Supplementary materials

Supplementary material associated with this article can be found, in the online version, at doi:10.1016/j.proci.2022.06.009.

References

[1] S.B.M. Deshmukh, A. Krishnamoorthy, V.K. Bhojwani, *Heat Transf. Res.* 50 (2019) 1023–1041.
[2] S.S. Merchant, C.F. Goldsmith, A.G. Vandeputte, M.P. Burke, S.J. Klippenstein, W.H. Green, *Combust. Flame* 162 (2015) 3658–3673.
[3] J Qi, M.Z. Liao, C. Wang, et al., *Int. J. Hydrog. Energy* 45 (2020) 8941–8954.
[4] M.G. Waller, M.R. Walluk, T.A. Trabold, *J. Power Sources* 274 (2015) 149–155.
[5] M. Huff, P.M. Torniainen, D.A. Hickman, L.D. Schmidt, *Natural Gas Conversion II* (1994) 315–320.
[6] H. Pennemann, V. Hessel, G. Kolb, H. Lowe, R. Zapf, *Chem. Eng. J.* 135 (2008) S66–S73.
[7] V. Subramanian, J.U. Choi, E.G. Seebauer, R.I. Masel, *Catal. Letters* 113 (2007) 13–18.
[8] B. Silberova, H.J. Venvik, A. Holmen, *Catal. Today* 99 (2005) 69–76.
[9] D. Pagani, D. Livio, A. Donazzi, et al., *Catal. Today* 197 (2012) 265–280.
[10] A. Donazzi, D. Livio, C. Diehm, A. Beretta, G. Groppi, P. Forzatti, *Appl. Catal. A- Gen.* 469 (2014) 52–64.
[11] A. Donazzi, D. Livio, M. Maestri, et al., *Angew. Chem. Int. Ed. Engl.* 50 (2011) 3943–3946.
[12] M. Hettel, C. Diehm, B. Torkashvand, O. Deutschmann, *Catal. Today* 216 (2013) 2–10.
[13] T.A. Wierzbicki, I.C. Lee, A.K. Gupta, *Appl. Energy* 130 (2014) 350–356.
[14] C. Karakaya, H. Karadeniz, L. Maier, O. Deutschmann, *ChemCatChem* 9 (2017) 685–695.
[15] R. Sui, J. Mantzaras, R. Bombach, *Proc. Combust. Inst.* 36 (2017) 4313–4320.
[16] A. Schneider, J. Mantzaras, R. Bombach, S. Schenker, N. Tylli, P. Jansohn, *Proc. Combust. Inst.* 31 (2007) 1973–1981.
[17] J. Mantzaras, R. Sui, C.K. Law, R. Bombach, *Proc. Combust. Inst.* 38 (2021) 6473–6482.
[18] J. Mantzaras, *Prog. Energy Combust. Sci.* 70 (2019) 169–211.
[19] R. Sui, E.T. Es-Sebbar, J. Mantzaras, R. Bombach, *Combust. Flame* 180 (2017) 184–195.
[20] R. Sui, J. Mantzaras, R. Bombach, *Combust. Flame* 202 (2019) 292–302.
[21] San Diego Chemical reaction mechanism, 2022. 2016-12-14, https://web.eng.ucsd.edu/mae/groups/combustion/mechanism.html.
[22] M.E. Coltrin, R.J. Kee, F.M. Rupley, *Surface Chemkin: A Fortran Package For Analyzing Heterogeneous Chemical Kinetics At the Solid Surface-Gas Phase interface, Report No. SAND90-8003C*, Sandia National Laboratories, 1996.
[23] R.J. Kee, F.M. Rupley, J.A. Miller, *Chemkin II: A Fortran Chemical Kinetics Package For the Analysis of Gas-Phase Chemical kinetics, Report No. SAND89-8009B*, Sandia National Laboratories, 1996.
[24] R.J. Kee, G. Dixon-Lewis, J. Warnatz, M.E. Coltrin, J.A. Miller, *A Fortran computer Code Package For the Evaluation of Gas-Phase Multicomponent Transport properties, Report No. SAND86-8246*, Sandia National Laboratories, 1996.
[25] D.I. Shin, T. Dreier, J. Wolfrum, Appl. Phys. B-Lasers Op*t* 72 (2001) 257–261.

[26] S. Werle, R.K. Wilk, *Fuel* 89 (2010) 1833–1839.
[27] R. Sui, J. Mantzaras, Z. Liu, C.K. Law, *Combust. Flame* (2022) article in press, doi:10.1016/j.combustflame.2021.111847.
[28] A.E. Lutz, R.J. Kee, J.A. Miller, *SENKIN: A Fortran Program For Predicting Homogeneous Gas Phase Chemical Kinetics With Sensitivity analysis, Report No. SAND87-8248*, Sandia National Laboratories, 1996.
[29] S. Eriksson, A. Schneider, J. Mantzaras, M. Wolf, S. Järås, *Chem. Eng. Sci.* 62 (2007) 3991–4011.